

Large-Grained Perovskite Films Enabled by One-Step Meniscus-Assisted Solution Printing of Cross-Aligned Conductive Nanowires for Biodegradable Flexible Solar Cells

Jiabin Qi, Shuo Chen, Chuntao Lan, Aurelia Chi Wang, Xun Cui, Zhengwei You, Qinghong Zhang,* Yaogang Li, Zhong Lin Wang, Hongzhi Wang,* and Zhiqun Lin*

Increasing performance demand associated with the short lifetime of consumer electronics has triggered fast growth in electronic waste, leading to serious ecological challenges worldwide. Herein, a robust strategy for judiciously constructing flexible perovskite solar cells (PSCs) that can be conveniently biodegraded is reported. The key to this strategy is to capitalize on meniscus-assisted solution printing (MASP) as a facile means of yielding cross-aligned silver nanowires in one-step, which are subsequently impregnated in a biodegradable elastomeric polyester. Intriguingly, the as-crafted hybrid biodegradable electrode greatly constrains the solvent evaporation of the perovskite precursor solution, thereby generating fewer nuclei and in turn resulting in the deposition of a large-grained dense perovskite film that exhibits excellent optoelectronic properties with a power conversion efficiency of 17.51% in PSCs. More importantly, the hybrid biodegradable electrode-based devices also manifest impressive robustness against mechanical deformation and can be thoroughly biodegraded after use. These results signify the great potential of MASP for controllably assembling aligned conductive nanomaterials for biodegradable electrodes. As such, it represents an important endeavor toward environmentally friendly, multifunctional and flexible electronic, optoelectronic, photonic, and sensory materials and devices.

1. Introduction

The past decade has witnessed accelerated development of perovskite solar cells (PSCs) with power conversion efficiency

(PCE) leaping from $\approx 3\%$ to a certified value of 25.2%,^[1] exceeding or comparable to those of other photovoltaics, including CdTe, copper indium gallium selenide (CIGS), and silicon-based solar cells. To date, PSCs have been generally fabricated on conductive glass (e.g., fluorine-doped tin-oxide (FTO) glass) or plastic substrates (e.g., indium-tin-oxide (ITO)-coated polyethylene terephthalate (PET); denoted ITO-PET). Notably, these two electrodes cannot be easily recycled, and the plastics-based substrates derived from petroleum are not eco-friendly. Moreover, with significant progress in PSCs and short device lifetime, tremendous need for conductive substrates may result in the generation of a large amount of waste and rapid consumption of rare elements (e.g., indium in FTO/ITO and gallium in gallium-doped zinc oxide glass). This places high demand on the supply of rare elements and greatly impacts the environment in the near future, and on the other hand, it motivates the development of environment-friendly PSCs.^[2] Although

green solvents (e.g., methanol (MeOH), ethanol (EtOH), and isopropanol (IPA)) have been widely used for processing large-area perovskite films,^[3] very limited work on biodegradable perovskite-based devices have been reported.^[4] On the other hand, flexible electrodes derived from biodegradable materials represent a promising candidate for many emerging and eco-friendly applications.^[5,6] However, their implementation in PSCs have yet to be explored.

Because of their low sheet resistance (R_s) and high optical transmittance (T) compared to other materials (e.g., graphene,^[7] conducting polymers,^[8] and carbon nanotubes^[9]), silver nanowires (Ag NWs) have attracted tremendous interest for conductive electrodes by a broad range of solution-based processes, including spin coating,^[10] spray coating,^[11] and vacuum filtration.^[12] However, these approaches often assemble Ag NWs into a random network, leading to the inhomogeneity, junction resistance between NWs, entanglement among NWs, and surface roughness of NWs.^[13,14] It is notable that a delicate balance between electrical conductivity and optical transmittance of Ag NWs is the key to their use in electronics.^[15] As a result, it

J. Qi, C. Lan, A. C. Wang, Dr. X. Cui, Prof. Z. L. Wang, Prof. Z. Lin
School of Materials Science and Engineering
Georgia Institute of Technology
Atlanta, GA 30332, USA
E-mail: zhiqun.lin@mse.gatech.edu

J. Qi, S. Chen, C. Lan, Prof. Z. You, Prof. Q. Zhang,
Prof. Y. Li, Prof. H. Wang
State Key Laboratory for Modification of Chemical Fibers
and Polymer Materials
College of Materials Science and Engineering
Donghua University
Shanghai 201620, P. R. China
E-mail: zhangqh@dhu.edu.cn; wanghz@dhu.edu.cn

The ORCID identification number(s) for the author(s) of this article can be found under <https://doi.org/10.1002/aenm.202001185>.

DOI: 10.1002/aenm.202001185

remains challenging to develop flexible electrodes that concurrently exhibit high electrical conductivity, outstanding optical transmission, and low surface roughness.^[16]

Herein, we report a simple yet highly effective strategy (i.e., meniscus-assisted solution printing (MASP)) to craft crossly aligned Ag NWs followed by their impregnation in biodegradable elastomeric polyester (i.e., forming hybrid biodegradable electrode), which impart the growth of large-grained perovskite film for flexible, mechanically robust, biodegradable, and high-performance PSCs. The MASP strategy involves the constraint of the Ag NW solution between two parallel plates with the upper stationary plate and the lower movable substrate placed on a computer-controlled translation stage. Strikingly, by adjusting the distance between the upper and lower plates, the MASP technique renders *one-step* creation of cross-aligned Ag NWs comprising horizontally oriented Ag NWs dictated by the hydrodynamic force owing to the moving substrate and vertically oriented Ag NWs regulated by the “stick-and-slip” motion of the three-phase contact line at which Ag NWs experience. Notably, the hybrid biodegradable electrodes display comparable electrical conductivity as commercially available flexible ITO-PET film without sacrificing optical transparency due to the orthogonally aligned Ag NWs. More importantly, they also demonstrate substantially enhanced electrical conductivity (52.6 Ω per square) over randomly dispersed Ag NWs obtained by spray-coating (20.8 k Ω per square) at 90% transparency, representing three orders of magnitude improvement. Intriguingly, in the process of depositing perovskite film onto the electron-transport-layer-coated hybrid biodegradable electrode for PSCs, the evaporation of perovskite precursor solution is restricted in the space imposed by cross-aligned Ag NWs. Consequently, compared to flat ITO-PET electrode used as control, confined evaporation of perovskite precursor solution yields a reduced number of nuclei, thereby leading to the formation of a dense large-grained perovskite film. The resulting flexible PSCs manifest excellent optoelectronic properties with a *PCE* of 17.51% (comparable to *PCE* of 16.86% for ITO-PET-based devices) as well as appealing mechanical robustness against bending. More importantly, the PSCs can be quickly degraded in the lipase water solution, leaving behind recyclable Ag NWs. Clearly, the MASP strategy enables rapid preparation of cross-aligned conductive NWs for hybrid biodegradable electrodes, opening up a new avenue for developing environmentally friendly electronics and optoelectronics (e.g., *green* PSCs, LEDs, photodetectors, etc.).

2. Results and Discussion

Poly(glycerol sebacate urethane) (PGSU), a biodegradable elastomeric polyester, possesses covalently crosslinked three-dimensional structure.^[17] Due to its high transparency, good hydrophilicity, and excellent solution processibility,^[18] PGSU can be developed as a unique biodegradable hybrid electrode containing various conductive nanomaterials to further expand its application in flexible electronics. This, however, has yet to be implemented in PSCs. As a tough, biocompatible, and biodegradable polymer, PGSU can be readily synthesized via a two-step reaction, as depicted in **Figure 1a**. First, poly(glycerol

sebacate) (PGS) was synthesized via a polycondensation reaction of glycerol and sebacic acid at an 1:1 molar ratio over 48 h (hereafter referred to as PGS pre-polymer). The weight-average of PGS pre-polymer was 12700 ± 1600 g mol⁻¹ with a polydispersity index of 4.5 ± 0.5 (see Experimental Section in Supporting Information). The structure of pre-polymer was characterized using NMR (Figure S1, Supporting Information). In addition, Figure S2 (Supporting Information) shows the elasticity of as-prepared PGS after thermal curing (partially crosslinked due to the reaction between the free hydroxyl groups in PGS pre-polymer and the carboxyl group in residual sebacic acid) evaluated by cyclic mechanical testing. The tensile strength of PGS is too low (≈ 1.5 kPa) to be employed as the substrate for solar cells. Therefore, it needs to be crosslinked to improve its tensile strength. To this end, aliphatic hexamethylene diisocyanate (HDI) was selected as the crosslinking agent due to its low-cost and extensive use in the synthesis of biodegradable and biocompatible ester-containing polyurethanes.^[19] The rapid reaction between the exposed free hydroxyl groups at the end of partially crosslinked PGS pre-polymer chain and the isocyanate groups in HDI under mild conditions yields three-dimensional, covalently crosslinked network via the formation of urethane linkages (i.e., producing poly(glycerol sebacate urethane) (PGSU); lower right chemical structure in Figure 1a). Figure 1b shows the FTIR spectrum of PGSU, signifying the success in the synthesis of PGSU. The free hydroxyl groups in PGS pre-polymer has a broad peak appeared at 3445 cm⁻¹, corresponding to the -OH stretching.^[20] After reacting with HDI, the resulting urethane groups lead to a peak shift to a lower wavenumber (3332 cm⁻¹), corresponding to the -NH- group stretching. Moreover, the peak centered at 1735 cm⁻¹ can be assigned to the stretching of the carbonyl group (-CO-) in PGSU. The urethane bond (-NH-COO-) at 1560 cm⁻¹ can also be seen in PGSU, further verifying the formation of urethane linkages in the backbone of PGSU. In addition, the peak at 2270 cm⁻¹ can be ascribed to the characteristic stretching of the isocyanate group, suggesting the presence of unreacted HDI. We note that the residual HDI can react with moisture to yield carbon dioxide and have no effect on the properties of PGSU.^[21] More interestingly, Figure 1c shows the markedly improved tensile strength (16.9 MPa) of PGSU film over that of the thermally cured, ester-linkage-containing PGS, due largely to the formation of additional urethane linkages. This produces a three-dimensional, covalently crosslinked network, which effectively strengthens the chemical bonding among polymer chains and thus mechanical properties.^[22] The contact angle of the PGSU film is $53.19^\circ \pm 3.2^\circ$, indicating a good hydrophilicity.

Subsequently, the PGSU was used to prepare transparent and conductive electrodes. Figure 1d depicts the procedure for the flexible, hybrid, and biodegradable Ag NWs/PGSU electrode. First, zinc oxide (ZnO) film with an average room mean square roughness, *Ra* of 4.97 nm (Figure S3, Supporting Information) was deposited on a glass substrate. Subsequently, the MASP of Ag NWs ethanol solution yielded the cross-aligned Ag NWs. Specifically, a drop of Ag NWs ethanol solution was loaded in a two-nearly parallel-plate geometry of a certain separation distance (*H*) with the upper plate fixed while the lower plate (i.e., ZnO-coated glass substrate) placed on a computer-controlled translational stage and moved at a constant velocity,

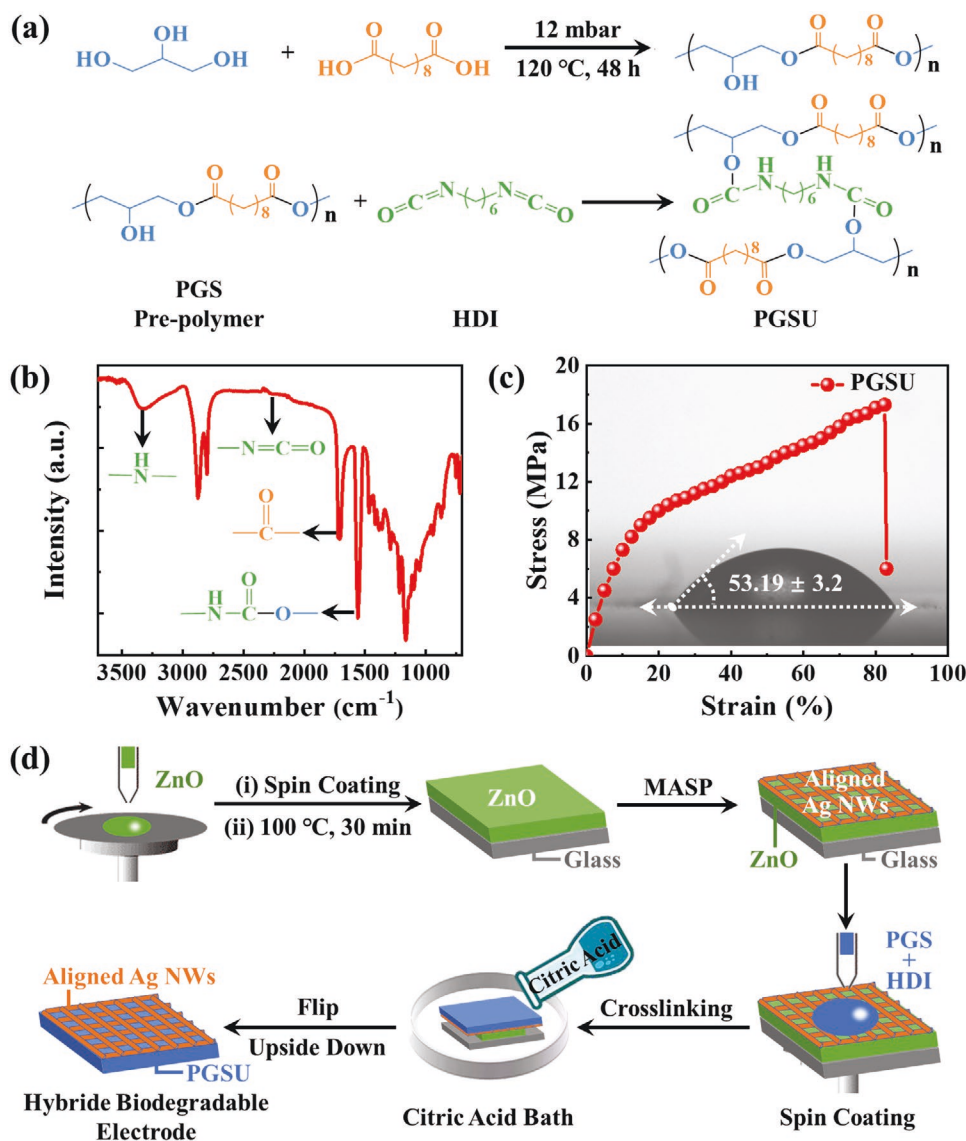


Figure 1. a) Reaction schemes of poly(glycerol sebacate) (PGS) pre-polymer and poly(glycerol sebacate urethane) (PGSU). b) FTIR spectrum of PGSU. c) Representative stress-strain curve and contact angle measurement of PGSU film (inset). d) Schematic illustration of fabrication procedure for flexible, hybrid, and biodegradable electrodes containing cross-aligned Ag NWs impregnated in PGSU film. A ZnO film is predeposited on glass. Then, the meniscus-assisted solution printing (MASP) of Ag NWs yields cross-aligned Ag NWs, followed by spin-coating the PGS pre-polymer and hexamethylene diisocyanate (HDI) and dissolving sacrificial ZnO layer in citric acid solution to produce flexible, hybrid Ag NWs/PGSU electrode that can be conveniently degraded by lipase.

as illustrated in **Figure 2a**. Notably, a meniscus is formed at the edge of the confined Ag NWs solution (**Figure 2a**). The programmable moving of ZnO-coated glass substrate results in a one-step creation of cross-aligned Ag NWs that will be discussed later. Nonetheless, the PGS pre-polymer and HDI mixture were then spun onto as-obtained cross-aligned Ag NWs, followed by selective etching of underlying sacrificial ZnO film using 10 wt% citric acid DI water solution, leading to free-standing flexible, hybrid, and biodegradable Ag NWs/PGSU electrode (**Figure 1d**). **Figure 2b** shows the digital image of as-prepared Ag NWs/PGSU film with a high homogeneity over an area of $1.5 \times 2.5 \text{ cm}^2$. We note that the Ag NWs/PGSU film has the same tensile strength (16.9 MPa) as the PGSU film, mainly

because the Ag NWs layer is very thin due to the monolayer orthogonality, thus has little effect on the mechanical property of the film. As surface roughness plays a crucial role in utilizing Ag NWs/PGSU as the hybrid electrode for PSCs, atomic force microscopy measurement was performed, showing a low average surface roughness of $R_a \approx 2.77 \text{ nm}$ (**Figure S4**, Supporting Information). This value is much smaller than most of previously reported Ag NW-network-based electrodes (e.g., 18–23 nm).^[23,24] The Ag NWs/PGSU electrode also exhibited a good bending stability, as will be discussed later, which is due to the increased adhesion by impregnating Ag NWs in biodegradable elastomeric polyester. The excellent performances noted above demonstrate that the sacrificial layer is indispensable in

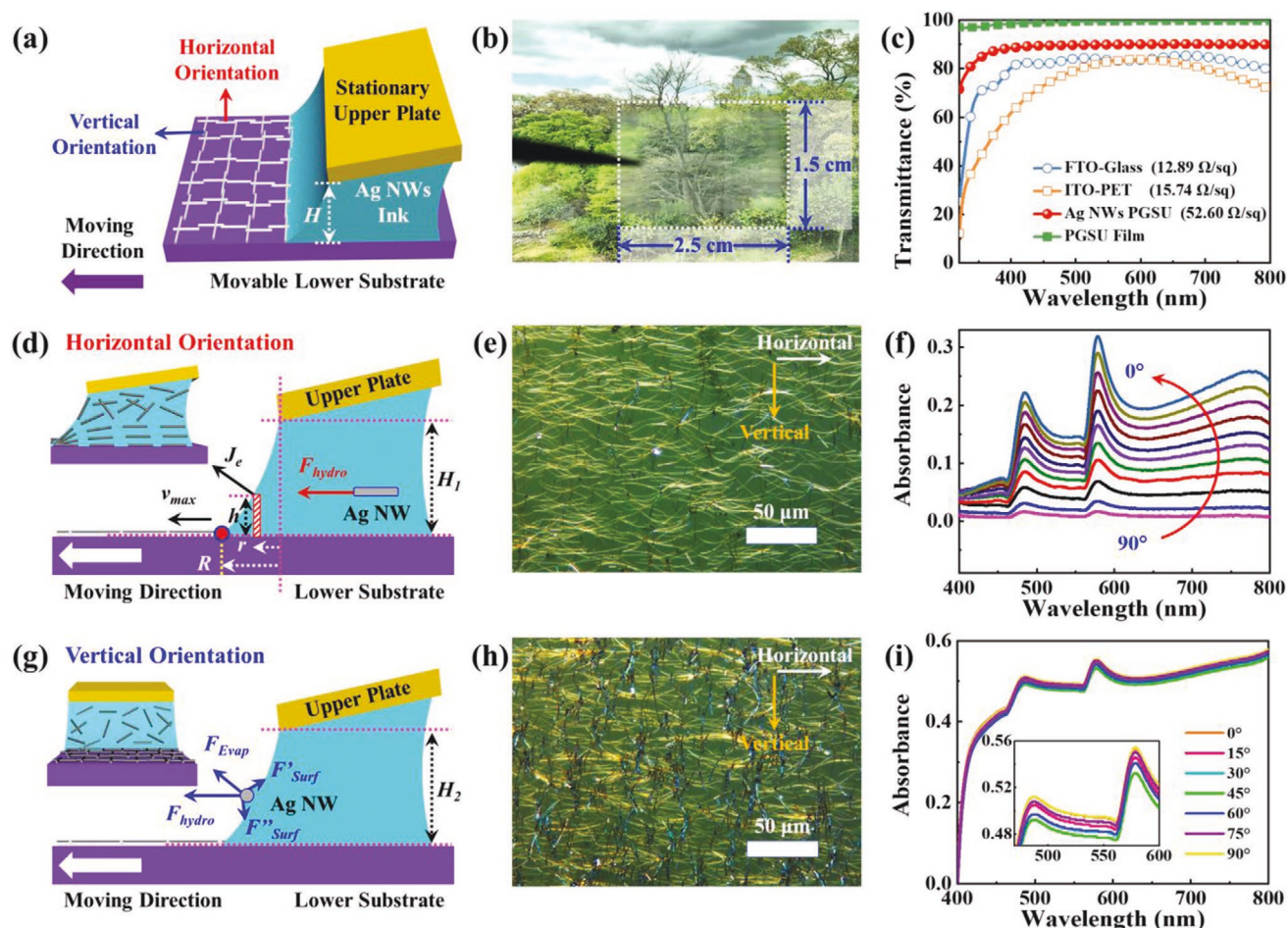


Figure 2. a) Schematic of the formation of cross-aligned Ag NWs during the MASP process. b) Optical micrograph of as-prepared electrode with excellent transparency (size = $1.5 \times 2.5 \text{ cm}^2$). c) Optical transmittance as a function of wavelength for various electrodes of different sheet resistances. d) Schematic of confined solution between two-nearly parallel plates (side view) with parameters labeled to account for horizontal alignment of Ag NWs. Inset: schematic of the distribution of Ag NWs at the meniscus and in bulk solution (side-view). e) SEM image of a majority of horizontal-aligned Ag NWs. f) Polarized UV-vis absorption spectra of a majority of horizontal-aligned Ag NWs as a function of polarization angle (0° – 90°). g) Schematic of confined solution for illustrating the vertical deposition of Ag NWs to yield cross-aligned Ag NWs. The forces at meniscus surface that an Ag NW experience is also depicted. Inset: schematic of the Ag NWs distribution at the meniscus surface. h) SEM image of cross-aligned Ag NWs. i) Polarized UV-vis absorption spectra of cross-aligned Ag NWs.

the preparation process. In addition, the Ag NWs/PGSU film has appealingly high transparency with $\approx 90\%$ transmittance at 550 nm, outperforming that of commercially available ones (Figure 2c). It is worth noting that higher transmittance along with expanded wavelength range ensure more solar light to be absorbed by the photoactive perovskite layer in PSCs. Moreover, low surface roughness and small sheet resistance (52.60Ω) of Ag NWs/PGSU film are also beneficial for the fabrication of high-performance PSCs.

For comparison, a spray-coating of Ag NWs was also performed, yielding randomly distributed NWs on the glass substrate. Due to serious aggregation (Figure S5, Supporting Information) and large surface roughness (Figure S6, Supporting Information) of random dispersed Ag NWs network, it is very difficult to reach a balance between high optical transmittance and excellent electrical conductivity (Figure S7, Supporting Information), which is a prerequisite for transparent electrodes. In general, the increased conductivity of electrode has reduced

optical transmittance. Under the same electrical conductivity, the structure of orthogonally oriented Ag NWs can effectively improve the optical transmittance. In our study, we prepared the cross-aligned Ag NWs by the MASP strategy. In this process, the concentration of Ag NWs solution is critical. At the low concentration of Ag NWs solution, the Ag NWs cannot be in good contact with each other due to their small content, leading to the decreased conductivity of electrode. On the other hand, when the concentration of Ag NWs solution is high, it would largely affect the optical transmittance of electrode as noted above. Thus, the concentration of Ag NWs solution was set to be 0.1 mg mL^{-1} , rendering a balance between electrical conductivity and optical transmittance of the resulting Ag NWs/PGSU electrode.

We now turn our attention to rationalize *one-step* formation of orthogonal Ag NWs that are responsible for excellent transparency and good electrical conductivity of the resulting Ag NWs/PGSU electrode. As illustrated in Figure 2a, cross-aligned

Ag NWs comprise horizontal and vertical deposits. The horizontally oriented Ag NWs are driven by shear-induced hydrodynamic force on the confined Ag NWs ethanol solution due to continued moving of lower ZnO-coated glass substrate placed on the translational stage in a two-nearly parallel-plate geometry. To further analyze the shear-induced hydrodynamic force, a representative side-view schematic of the confined solution with meniscus is depicted in Figure 2d. We note that the velocity of the outward convective flow v induced by solvent evaporation can be given as follows:^[25,26]

$$v = \frac{1}{\rho r h} \int_0^r \left(\frac{r}{h + K + T} \right) dr \quad (1)$$

where ρ is the solution density, r is the horizontal distance between the meniscus surface and the bulk solution, h is the height of the meniscus at r , K is a non-equilibrium variable, and T is the thermal effect parameter^[26] (see Experimental Section in Supporting Information). Clearly, Equation (1) suggests that the outward convective flow is accelerated at the edge of meniscus, that is, v rapidly increases as r increases (i.e., when approaching the meniscus edge). As a result, the outward convective flow carries the Ag NWs to the front of the meniscus and aligns them at the edge. The relationship between shear-induced hydrodynamic force F_{hydro} and v can be given by the following equation,^[27]

$$F_{\text{hydro}} = \frac{4\pi\mu av}{\ln\left(\frac{2a}{b}\right) - 0.72} \quad (2)$$

where μ is the viscosity of the fluid ($\approx 15 \times 10^{-3}$ Pa s at 353.15 K for Ag NWs ink dissolved in ethanol), and a and b are the length (≈ 60 μm) and radius (≈ 50 nm) of Ag NWs. According to Equation (2), the maximum $F_{\text{hydro,max}}$ acting on Ag NWs exists at the very edge of the meniscus where $h = 0$ and r reaches the maximum value (Figure 2d), with which Ag NWs rapidly align horizontally, while Ag NWs situated within the meniscus away from $h = 0$ remain randomly populated due to the smaller F_{hydro} as depicted in the inset of Figure 2d. Assuming the maximum v at the very edge of the meniscus reaches the moving speed of the lower ZnO-coated glass substrate (i.e., 100 $\mu\text{m s}^{-1}$). The hydrodynamic force $F_{\text{hydro,max}}$ at the very edge can be estimated to be 1.5 nN, which is sufficient to align Ag NWs (≈ 0.8 nN).^[28]

Figure 2e presents an optical micrograph of the massively horizontal-aligned Ag NWs in conjunction with some vertical-aligned Ag NWs (as discussed later). The alignment of Ag NWs is clearly evident in the AFM image (Figure S8, the corresponding cross-section analysis of several Ag NWs and an individual Ag NW are shown in Figure S9, Supporting Information). The horizontal-aligned Ag NWs possess anisotropic optical properties. The subtle differences in the UV-vis absorption spectra (i.e., (a) and (b) in Figure S10 from 400 to 800 nm, Supporting Information) indicate that the polarized absorption spectra of the horizontal-aligned Ag NWs is correlated to the polarization angle θ ($\theta = 0^\circ$ – 90° , defined as the angle between the polarization direction of incident light and the direction of aligned Ag NWs; Figure S11, Supporting Information). It is noteworthy that the absorption peak intensity decreases as

θ increases, suggesting that the majority of Ag NWs aligned along the moving direction of polarizing filter (see curve at $\theta = 0^\circ$) yet still contained a small population of vertical-aligned Ag NWs (see curve at $\theta = 90^\circ$) (Figure 2f). In sharp contrast, no obvious changes in the absorbance of randomly dispersed Ag NWs network were seen (i.e., no optical anisotropy with increasing polarization angle θ).^[29]

A small amount of vertical-aligned Ag NWs yet coexisted with the majority of horizontal-aligned counterparts (Figure 2e) can be justified as follows. As depicted in Figure 2g, Ag NWs in the upper part of trapped solution will reach the curved meniscus surface due to the movement of lower ZnO-coated glass substrate. A competition between a surface tension-related depinning force (F_{surf}) and a pinning forces due to solvent evaporation ($F_{\text{evap}} = \frac{J_e}{h} l$, where l is the length of Ag NW)^[30] and fluid motion (F_{hydro}) drives the randomly oriented Ag NWs at the curved meniscus surface to move toward the very edge of the meniscus (i.e., three-phase contact line formed by the Ag NWs ethanol solution, lower ZnO-coated glass substrate, and air) (Figure 2e). Consequently, each individual Ag NW is vertically deposited on lower ZnO-coated glass substrate driven by the maximization of interfacial interaction (i.e., contact) between the Ag NW and the substrate at the three-phase contact line (a well-known “coffee ring” effect^[31]). Moreover, the formation of stripe-like vertically aligned Ag NWs is a consequence of repetitive “stick-and-slip” motion of the three-phase contact line caused by the continuous moving of the lower ZnO-coated glass substrate. As the lower substrate was moved at a constant speed, the meniscus was stretched and the initial contact angle θ_i at the meniscus edge (Figure 2g) decreased to a critical value θ_c . At θ_c , the depinning force became larger than the pinning force,^[32] leading to the jump of the contact line to a new position (i.e., “slip”) where the θ_i was resumed, thus forming a new Ag NWs stripe. The repetitive “stick-and-slip” cycles of the three-phase contact line yielded a set of periodic stripes. It is also interesting to note that the larger the separation distance H between the upper plate and lower substrate (Figure 2a) is, the more Ag NWs will be exposed at the meniscus surface, thereby resulting in a denser vertical deposition at the fixed Ag NWs solution concentration, as clearly evidenced in Figure 2e (sparsely populated vertical-aligned Ag NWs at $H_1 = 100$ μm) and Figure 2h (dense vertical-aligned Ag NWs at $H_2 = 300$ μm). Compared to a vast majority of horizontal-aligned Ag NWs (Figure 2f), only slight changes in the absorption peaks were observed for largely cross-aligned Ag NWs. Taken together, judiciously tuning H in the MASP strategy render the control over the cross-alignment process of Ag NWs in a *one-step* manner for producing highly transparent and good conductive electrodes.

The highly transparent, conductive, and biodegradable Ag NWs/PGSU film was then used as electrode for PSCs fabricated via a substrate-transfer process using the fluorinated polymer as the release agent (Figure S12, Supporting Information). We note that the annealing process of tin dioxide (SnO_2) and perovskite film has no influence on the conductivity and plastic deformation of the Ag NWs/PGSU substrate due to the much lower annealing temperature (i.e., 100 $^\circ\text{C}$ for SnO_2 and 110 $^\circ\text{C}$ for perovskite film) than the onset thermal degradation temperature

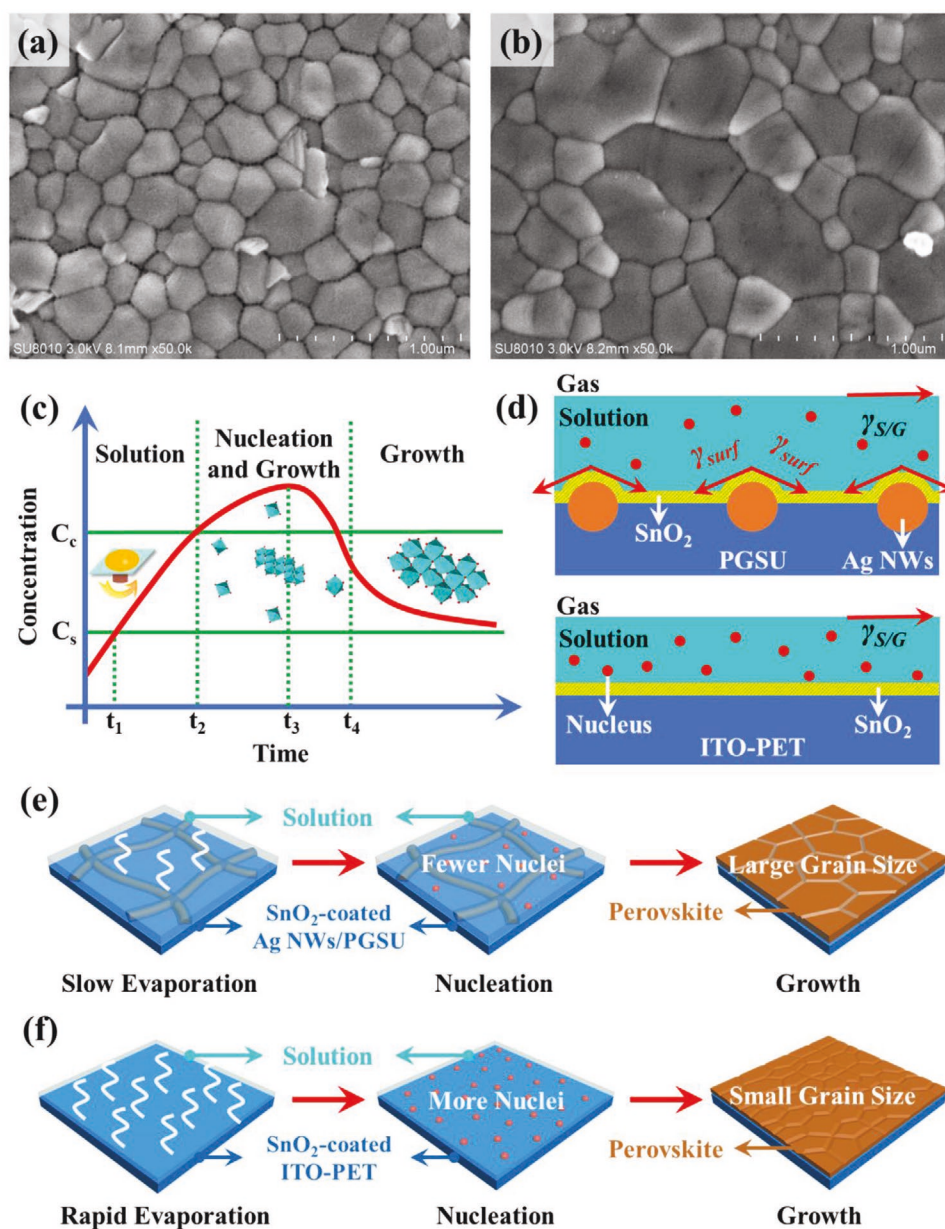


Figure 3. SEM image of perovskite films on a) SnO₂-coated ITO-PET (control sample) and b) SnO₂-coated Ag NWs/PGSU electrodes. c) The LaMer model accounting for nucleation and growth of perovskite crystals. d) Schematic illustration of perovskite precursor solution during the spin-coating process on SnO₂-coated Ag NWs/PGSU electrode (upper panel) and on SnO₂-coated ITO-PET (lower panel). $\gamma_{s/g}$ and γ_{surf} are the surface tensions at the solution/gas interface and at the solution/SnO₂-coated Ag NWs/PGSU interface, respectively. The downward surface tension γ_{surf} retards the solvent evaporation, leading to the formation of less nuclei. e, f) Stepwise representation of nucleation and grain growth of perovskite on (e) SnO₂-coated Ag NWs/PGSU electrode, and (f) SnO₂-coated ITO-PET electrode, respectively.

(290 °C) of the Ag NWs/PGSU electrode (Figure S13, Supporting Information). Figure S14 (Supporting Information) presents a cross-sectional SEM image of the Ag NWs/PGSU-based PSC. Notably, a layer of SnO₂ with a thickness of 110 nm was spin-coated at room temperature onto Ag NWs/PGSU followed by thermal annealing at 100 °C to function as an efficient electron-transporting layer (ETL) (see Experimental Section in Supporting Information). Figure S15 (Supporting Information) shows the SEM image of SnO₂-coated Ag NWs/PGSU, suggesting uniform coating of SnO₂, and the underlying cross-

aligned Ag NWs are also clearly evident. The average surface roughness of Ag NWs/PGSU slightly increased from 2.77 (Figure S4, Supporting Information) to 3.09 nm after the SnO₂ coating (Figure S16, Supporting Information). The perovskite with a complex stoichiometry of (FAPbI₃)_{0.85}(MAPbBr₃)_{0.15} was selected as photoactive layer, where MA and FA are methylammonium and formamidinium, respectively. A (FAPbI₃)_{0.85}(MAPbBr₃)_{0.15} film of 700 nm thick was spun onto the SnO₂ ETL-coated Ag NWs/PGSU electrode (see Experimental Section in Supporting Information). **Figure 3a,b** compares the SEM

images of the perovskite film on the SnO₂-coated ITO-PET (as control) and SnO₂-coated Ag NWs/PGSU electrodes; and the average grain size of perovskite on the latter electrode is comparatively larger, increasing from 180 nm for the former to 340 nm for the latter electrodes (Figure S17, Supporting Information). This in turn improved the optoelectronic properties as discussed later.

To further uncover the formation mechanism of large perovskite grains on Ag NWs/PGSU electrodes, it is critical to scrutinize the crystal nucleation and growth of the perovskite layer. This can be described by the well-known LaMer mechanism,^[33] as illustrated in Figure 3c, where C_s is the saturated concentration of solute, and C_c is the critical concentration (i.e., minimum concentration) of solute for nucleation which represents a limiting state of supersaturation.^[34] As solvent evaporates (from time $t = 0 \rightarrow t_1$), the solution concentration reaches C_s at t_1 . From $t_1 \rightarrow t_2$, no nuclei are generated as the nuclei form at the same rate as they dissolve. As the concentration of solute (i.e., perovskite precursors) increases to C_c at t_2 , a large number of nuclei are generated and grown.^[35] As the solvent evaporation continues ($t_2 \rightarrow t_3$), the perovskite precursor solution is concentrated and the nucleation rate of perovskite is accelerated. Nonetheless, further evaporation ($t_3 \rightarrow t_4$) increases the consumption of solute for the growth of the generated nuclei, eventually reaching C_c again at t_4 (i.e., the end of the nucleation stage). Afterward ($t > t_4$), the concentration of solution is progressively lowered owing to the continuous growth of the generated stable nuclei of perovskite, representing the formation of larger crystals (upper right inset in Figure 3c), as long as the concentration is greater than C_s .

In view of the low formation enthalpy of perovskite crystals and extremely rapid evaporation rate of solvent on the concentrated wet film produced during spin-coating, which results in a continuous increase of the concentration above C_s , the crystallization of perovskite film is potentially governed by the nucleation and growth stage ($t_2 \rightarrow t_4$). Hence, the nucleation rate represents the key factor controlling the crystallization of perovskite film. According to the classical LaMer mechanism, the nucleation rate can be described by the following Arrhenius-type equation:

$$\frac{dN}{dt} = A \exp\left(-\frac{\Delta G_c}{k_B T}\right) \quad (3)$$

where N is the number of nuclei, t is the time, A is a pre-exponential constant, k_B is the Boltzmann constant, and T is the temperature. ΔG_c is the critical Gibbs free energy of nucleation (i.e., activation energy), reflecting the energy barrier that nuclei need to overcome for steady growth without their dissolution.^[36] In general, a lower nucleation rate leads to a larger grain size, and the nucleation rate is dictated by ΔG_c . As depicted in Figure 3d, during the spin-coating of perovskite precursor solution, the downward surface tension (γ_{surf}) acting at the interface between the precursor solution and the SnO₂-coated Ag NWs/PGSU electrode is yielded due to the protrusion of the underlying Ag NWs, thereby slowing down the evaporation of the precursor solution. This in turn exerts a resistance to crystal nucleation (i.e., increasing of ΔG_c), and thus the number of nuclei largely reduces according to Equation (3) (central panel; Figure 3e). Consequently, a perovskite film containing large-sized grains is

resulted in (right panel; Figure 3e). In contrast, as the solvent rapidly evaporates from flat SnO₂-coated ITO-PET electrode, the solution concentration can be readily maintained above C_c and the nucleation rate is dramatically increased, leading to the formation of more nuclei and thus smaller crystal grains (Figure 3f).

The X-ray diffraction (XRD) patterns of as-fabricated perovskite films spin-coated on SnO₂-coated ITO-PET (control sample) and SnO₂-coated Ag NWs/PGSU electrodes are presented in Figure 4a. All the diffraction peak positions of the two films are consistent with the simulated XRD profile of a trigonal perovskite crystal with $P3m1$ space group.^[37] It is notable that each diffraction peak of the perovskite film on SnO₂-coated Ag NWs/PGSU is narrowed, indicating a significantly increased grain size of perovskite crystals, which is consistent with the SEM measurements (Figure 3a,b). Intrigued by the enlarged grains, we further investigated the optoelectronic properties of the perovskite films. Figure S18 (Supporting Information) shows that the perovskite layer on the SnO₂-coated Ag NWs/PGSU electrode had a slight increase in the absorption of visible light due to a thicker perovskite film (700 nm) compared to that on the SnO₂-coated ITO-PET (450 nm; Figure S19, Supporting Information) under the same experimental conditions. The calculated bandgap (Figure S20, Supporting Information) based on the absorption spectra (Figure S18, Supporting Information) are nearly the same, demonstrating that the chemical structure of perovskite was not changed^[38] regardless of depositing on two different electrodes.

Subsequently, the charge dynamics was evaluated by steady-state photoluminescence (PL) (Figure 4b) and time-resolved photoluminescence (TRPL) (Figure 4c) characterizations. Compared to that on SnO₂-coated ITO-PET electrode, the PL intensity on the SnO₂-coated Ag NWs/PGSU electrode was reduced, suggesting that electrons can be effectively extracted in the hybrid biodegradable Ag NWs/PGSU electrode coated with a SnO₂ ETL. The impressive electron extraction can be attributed to high-quality large-sized perovskite grains (i.e., low grain boundary density) and excellent electrical conductivity of Ag NWs (i.e., $5.69 \times 10^7 \text{ S m}^{-1}$ for Ag NWs as compared to $1.03 \times 10^2 \text{ S m}^{-1}$ for ITO film, thereby facilitating electron extraction). Figure 4c compares the TRPL spectra of perovskite films on two different electrodes by examining the emission peak at 775 nm, and all data recorded are longer than the instrument response function (IRF), as indicated. The fast decay time (τ_1) and slow decay time (τ_2) can be determined by fitting the data to an exponential decay (specific physical basis on the interpretation of the TRPL decay in terms of bi-exponential can be seen in the Supporting Note in Supporting Information). τ_1 is related to the quenching of charge carriers through transport to SnO₂ ETL,^[39] whereas τ_2 is attributed to the radiative recombination of free charge carriers before the charge collection.^[40] For the ITO-PET/SnO₂/perovskite film, τ_1 and τ_2 were found to be 2.44 ± 0.02 and 311.46 ± 4.93 ns, respectively. For the PGSU/Ag NWs/SnO₂/perovskite film, both τ_1 and τ_2 were reduced to 1.02 ± 0.01 and 58.27 ± 0.71 ns, respectively, signifying a faster charge transfer from the perovskite film to the hybrid biodegradable Ag NWs/PGSU electrode through the SnO₂ ETL. Apparently, most of the photogenerated carriers can be effectively collected by the electrode with a low recombination

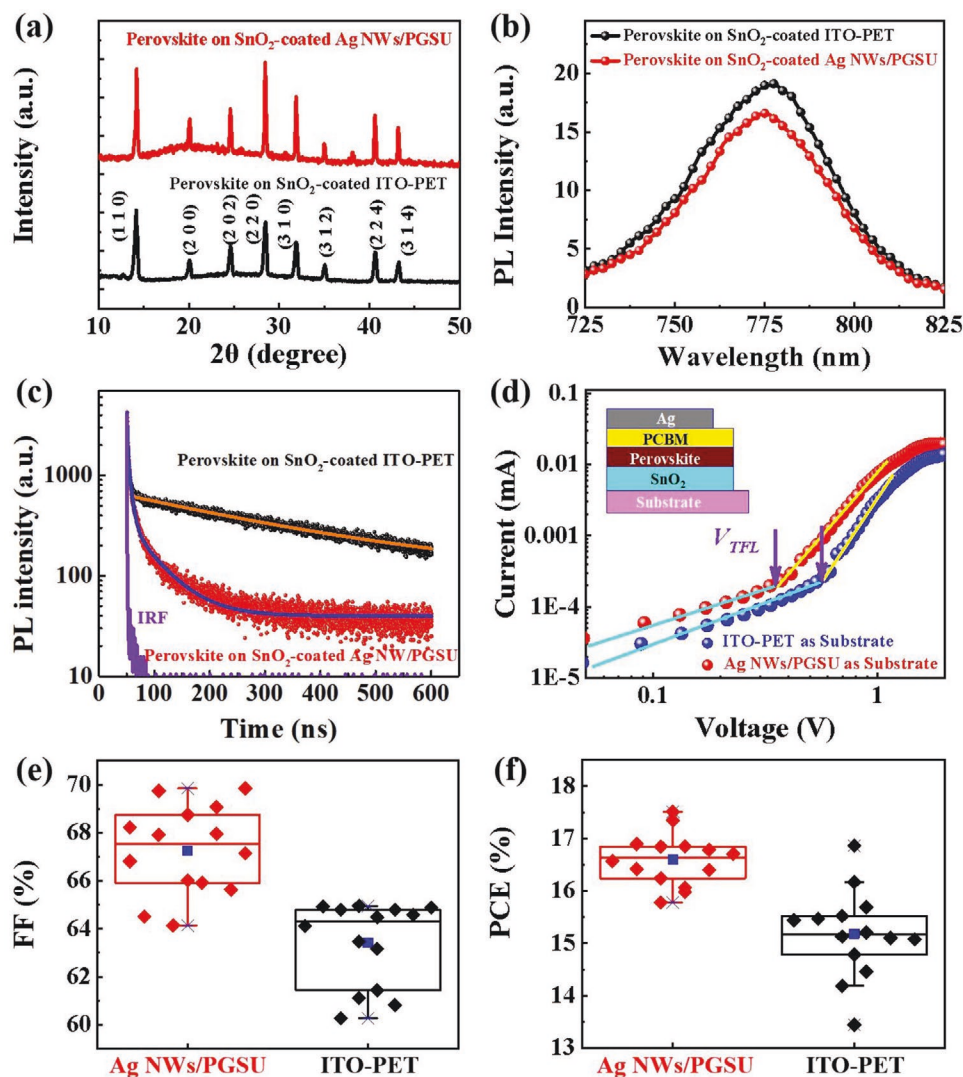


Figure 4. a) XRD patterns of perovskite films spin-coated on the SnO_2 -coated Ag NWs/PGSU electrode and the SnO_2 -coated ITO-PET electrode. b) Steady-state PL spectra and c) time-resolved PL (TRPL) spectra of perovskite films spun on the SnO_2 -coated Ag NWs/PGSU and the SnO_2 -coated ITO-PET electrodes, respectively. d) Dark I - V curves of electron-only devices showing trap-filled limit voltage (V_{TFL}). The inset shows the electron-only device architecture. Histograms of e) FF and f) PCE of devices constructed on the SnO_2 -coated Ag NWs/PGSU and the SnO_2 -coated ITO-PET electrodes, respectively.

loss. The rapid charge transfer (τ_1) and effective collection due to the reduced recombination (τ_2) in the PGSU/Ag NWs/ SnO_2 /perovskite grain size, in good accordance with the XRD and PL spectroscopy results. This in turn results in improved photovoltaic performance, including less hysteresis and higher fill factor (FF).^[41] The trap densities of perovskite deposited on two different substrates were also evaluated by constructing electron-only devices with the architecture of substrate/ SnO_2 /perovskite/phenyl-C61-butyric acid methyl ester (PCBM)/Ag (see Experimental Section in Supporting Information). Figure 4d presents the dark current-voltage (I - V) curves of the electron-only devices. The trap-filled limit voltage (V_{TFL}) is defined as the kink point of the bias voltage. At low bias voltage, the linear I - V curve (light blue line) reveals an Ohmic-type response. As the voltage increases above V_{TFL} , the current increases nonlinearly,

indicating completely filled traps. The trap density (N_{trap}) is correlated to V_{TFL} by the following equation:^[42]

$$N_{\text{trap}} = \frac{9\epsilon\epsilon_0 V_{\text{TFL}}}{eL^2} \quad (4)$$

where ϵ is the relative dielectric constant, ϵ_0 is the vacuum permittivity, and L is the film thickness. The trap density of perovskite film on SnO_2 -coated Ag NWs/PGSU electrode was estimated to be $2.23 \times 10^{15} \text{ cm}^{-3}$, approximately half of that on SnO_2 -coated ITO-PET electrode ($4.15 \times 10^{15} \text{ cm}^{-3}$). The lower trap density can be ascribed to the low grain boundary density and large crystal size of perovskite film on the SnO_2 -coated Ag NWs/PGSU electrode (Figure 3a,b). Taken together, the excellent structural and optoelectronic properties of such perovskite film offer the great potential to achieve high-performance PSCs.

To this end, PSCs composed of PGSU/Ag NWs/SnO₂/perovskite/Spiro-OMETAD/Ag were constructed. The devices using the SnO₂-coated ITO-PET electrode (i.e., ITO-PET/SnO₂/perovskite/Spiro-OMETAD/Ag) were also prepared and used as control. Figure S21 (Supporting Information) compares the current density–voltage (*J*–*V*) curves of the champion devices using the two different electrodes, demonstrating an open-circuit voltage (*V*_{OC}) of 1.08 V, short-circuit current density (*J*_{SC}) of 23.30 mA cm^{−2}, fill factor (*FF*) of 69.07%, and *PCE* of 17.51% under AM1.5 illumination for the SnO₂-coated Ag NWs/PGSU electrode-based device, and *V*_{OC} of 1.08 V, *J*_{SC} of 23.99 mA cm^{−2}, *FF* of 64.92%, and *PCE* of 16.86% for the SnO₂-coated ITO-PET electrode-based device. We note that these parameters were obtained from the reverse scan, and no appreciable difference was observed between the forward and reverse scans. Figure 4e,f presents the histograms of the *FF* and *PCE* values from 14 highly efficient and reproducible PSCs of different batches. Remarkably, a high *FF* was attained using the SnO₂-coated Ag NWs/PGSU electrode, which may be due to a good interfacial contact between the large-grained perovskite film and the SnO₂ ETL.^[43] Figure S22 (Supporting Information) shows a slight increase of *J*_{SC} and nearly unchanged *V*_{OC} of the SnO₂-coated Ag NWs/PGSU electrode-based devices (i.e., their distributions), compared to those of SnO₂-coated ITO-PET electrode-based counterparts. The unchanged *V*_{OC} can be attributed to the similar device structures (i.e., the alike band structure due to the same energy level (4.8 eV) of Ag NWs and ITO) and the same perovskite film in these two sets of devices, which is consistent with the calculated bandgap and the XRD results.^[44] The small increase of *J*_{SC} is due likely to the delicate balance between the enhanced *J*_{SC} because of the thicker perovskite film (700 nm) and the suppressed *J*_{SC} caused by the larger sheet resistance of electrode.^[45] Accordingly, the external quantum efficiency (EQE) spectra were integrated, and the resulting *J*_{SC} values for both types of devices were found to be in good agreement with the *J*–*V* curves (Figure S23, Supporting Information). Moreover, compared to the ITO-PET electrode, the Ag NWs/PGSU electrode has the higher transmittance (Figure 2c), which also contributed to the increasing *J*_{SC}. The improved photovoltaic performance of the SnO₂-coated Ag NWs/PGSU electrode-based devices can be attributed primarily to fast electron extraction due to high-quality large-sized perovskite grains (i.e., less grain boundaries) and excellent electrical conductivity of Ag NWs (Figure S24, Supporting Information). Finally, the *PCE*s of the devices fabricated using the SnO₂-coated Ag NWs/PGSU electrode shows promising advance over the state-of-the-art PSCs of various device structures, as summarized in Table S1 (Supporting Information), manifesting the tremendous potential of flexible hybrid Ag NWs/PGSU electrodes for use in PSCs.

The bending stability is one of the key quality indicators for flexible solar cells. Figure 5a displays the normalized *PCE* of flexible SnO₂-coated Ag NWs/PGSU-based PSCs measured after bending at different radii of curvature. The photographs of the corresponding bending tests are shown as the insets. After bending at a radius of curvature of 9.3 mm, the *PCE* remained the same without obvious degradation. Upon decreasing the bending radius to 5.5, 4.3, and 3.2 mm, the *PCE* progressively reduced to 15.73%, 14.80%, and 11.18%, respectively. The *J*–*V*

curves of flexible PSCs undergoing the bending are shown in Figure S25 (Supporting Information). Figure 5b summarizes the variations in the normalized *PCE*s when the flexible PSCs were deformed at different radii during the repeated bending cycles. The detailed parameters are listed Table S2 (Supporting Information). Notably, the PSCs retained a 93.2% of initial *PCE* at a bending radius of 9.3 mm after 500 bending cycles.

To identify the dominant factor governing the degradation of the optoelectronic performance, the resistance change of the Ag NWs/PGSU electrode as well as the morphology change of the perovskite film as a function of the bending cycles were further investigated. According to the previous report,^[46] ITO can be safely bent to a radius of 14 mm; yet below 14 mm, the ITO layer starts to crack, leading to significantly degraded conductivity. In contrast, the bending radius of our Ag NWs/PGSU electrode reaches 3.2 mm, only representing a slightly 6.5 Ω per square increase over that of initial state after 500 repeated bending cycles (Figure S26, Supporting Information), due primarily to the advantageous cross-aligned Ag NWs impregnated in the PGSU substrate. Meanwhile, the surface morphology changes of perovskite films were also studied after multiple bending cycles (Figure S27, Supporting Information). Under the same bending radius (i.e., 3.2 mm), with the increase of bending times (from 0 to 500 cycles), more and more cracks were emerged on the surface of perovskite film, which is unfavorable to the effective output performance of the whole device. In this case, the lower *J*_{SC} and *FF* of the flexible PSCs after repeated cycles of bending (Table S2, Supporting Information) were resulted likely from the fracture of the perovskite layer and the higher sheet resistance of the entire device after bending.^[47]

In addition, the long-term stability of the as-prepared PSCs was also investigated. The device without encapsulation was kept in a desiccator and the photovoltaic properties (Table S3, Supporting Information) were measured at an interval of several days. The device revealed no obvious reduction in *PCE* within 20 days (inset in Figure S28, Supporting Information), while a nearly 56% decrease of *PCE* was observed after 55 days (Figure S28, Supporting Information). We note that the Ag NWs/PGSU electrode can be stored without any degradation while retaining the transmittance and conductivity in natural environment (i.e., the absence of lipase) for at least 6 months. Thus, the attenuation in long-term optoelectronic performance is due primarily to the moisture-induced degradation of the perovskite layer when taking the device out of desiccator and measuring the *I*–*V* curves in air. In this case, we tested the moisture stability of perovskite films by exposing them to air with a 65% humidity. The moisture can decompose the perovskite into its precursors, during which the black perovskite film changes into the yellow lead iodide film. The moisture stability of both perovskite films on SnO₂-coated Ag NWs/PGSU electrode and SnO₂-coated ITO-PET electrode is shown in Figure S29 (Supporting Information). Clearly, the device encapsulation to isolate them from moisture and thus prevent it from life loss as well as the toxicity owing to the Pb leaking is needed for the practical application in the future.

Figure 5c presents the degradation process of flexible SnO₂-coated Ag NWs/PGSU-based PSCs. The lipase (from thermomyces lanuginosus) aqueous solution at a concentration of 10 000 U mL^{−1} was used in our study. When the device was

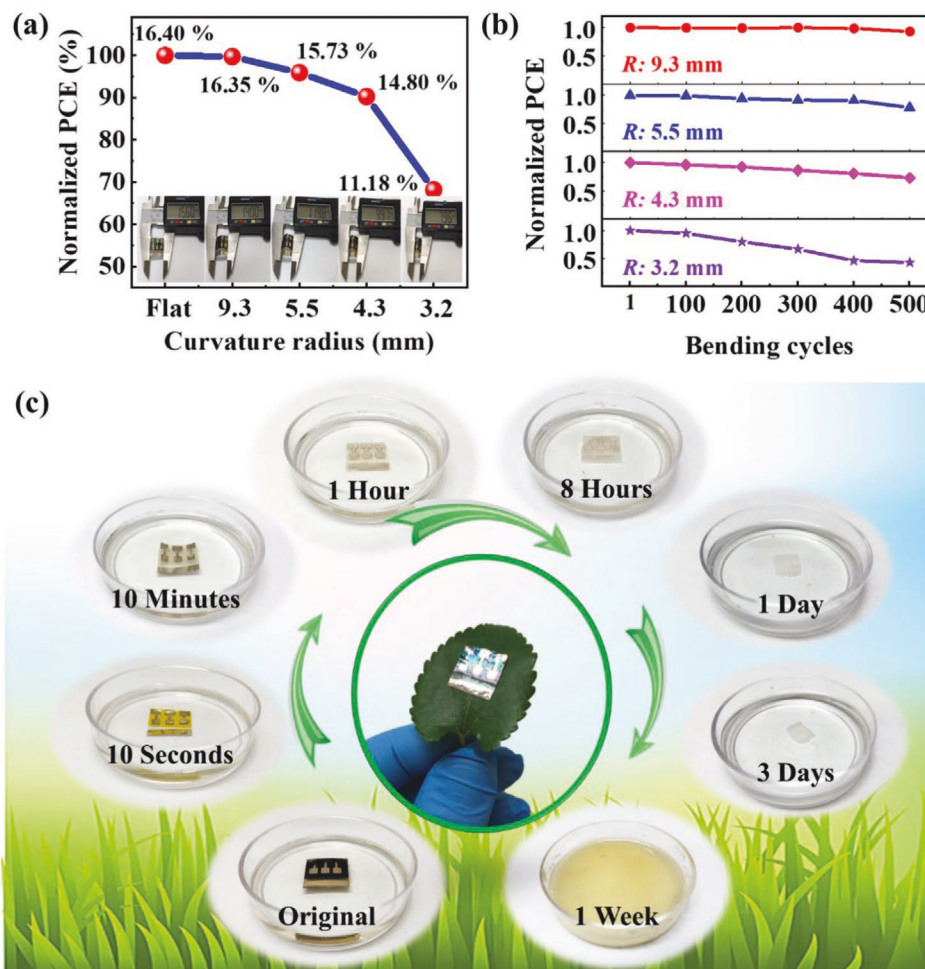


Figure 5. a) Normalized *PCE* measured after bending at different radii of curvature. b) Changes in normalized *PCEs* of flexible PSCs during 500 repeated bending cycles. c) Photographs of a PSC at various stages of biodegradation by lipase.

placed into the solution, it floated on the solution surface due to its light weight (≈ 15 mg; see *Original* in Figure 5c). Thus, it was pushed to be immersed underwater, and the cell color instantly changed from the original dark black to yellow in 10 s because of the decomposition of the perovskite layer in water. In the next 10 min, the perovskite layer was completely dissolution by lipase, leaving behind an Ag electrode on the PGSU substrate. Then, the Ag electrode slowly delaminated off, owing largely to the effect of bubbles produced from the biodegradation of the PGSU substrate (Figure S30, Supporting Information). After washing away the lipase attached to the surface, we clearly observed that the area of the PGSU substrate gradually decreased on a daily basis and completely disappeared within a week. The mechanism of PGSU degradation lies in the cleavage of the ester linkages, resulting in the production of glycerol, sebacic acid, and polyurethane segment.^[48] Glycerol and sebacic acid are both bio-based chemicals that widely exist in the nature and exhibit well-documented biocompatibility.^[49] Thus, PGSU exemplifies an excellent recyclable material. The lead (Pb) element in solution can be removed or recycled using proper waste treatment technology.^[50] As such, our devices are unlikely to present potential hazards to the environment, thereby

facilitating a broader range of environmentally friendly applications in energy conversion and storage, such as new energy vehicles, smart clothing, etc.

3. Conclusion

In summary, we developed a viable meniscus-assisted solution printing (MASP) strategy to *one-step* create cross-aligned Ag NWs that are subsequently integrated with biodegradable elastomeric polymer as flexible hybrid electrode for high-efficiency and *green* PSCs. The mechanism governing the formation of orthogonal Ag NWs by MASP is uncovered, that is, hydrodynamic force-driven parallel alignment of Ag NWs due to the moving of the lower substrate in conjunction with the “stick-and-slip” motion of three phase contact line-enabled perpendicular alignment of Ag NWs. Nonetheless, the hybrid electrode displays a set of appealing features, including high electrical conductivity (i.e., a low sheet resistance of 52.60Ω per square), small surface roughness (≈ 2.77 nm), and outstanding optical transmittance ($\approx 90\%$). More importantly, such the hybrid biodegradable electrode imparts the formation of a dense, crystalline

perovskite film with larger grains. This is due to the reduced evaporation of the perovskite precursor solution because of the downward surface tension exerted at the precursor solution/electrode interface, which leads to the formation of a decreasing number of nuclei and thus increased grain sizes of perovskite. The perovskite film on the hybrid electrode exhibit attractive optoelectronic properties with a high *PCE* of 17.51% in the resulting PSCs. The devices also carry good bending performance, demonstrating a 93.2% retention of initial *PCE* at a bending radius of 9.3 mm after 500 bending cycles. They can also be conveniently and thoroughly biodegraded in a week. Conceivably, as the diversity of nanomaterials (e.g., carbon nanotubes, graphene, 2D materials) are amenable to the MASP strategy and an array of biomaterials (e.g., protein, polysaccharides, etc.) other than synthetic polymers can be used as environmentally friendly substrates, the MASP technique affords a powerful platform to create a rich variety of biodegradable electrodes for a wide range of applications in multifunctional flexible optics, electronics, and optoelectronics.

Supporting Information

Supporting Information is available from the Wiley Online Library or from the author.

Acknowledgements

This work was supported by the NSF (CMMI 1727313; ECCS 1914562). The authors also acknowledge the financial support by Natural Science Foundation of China (No. 51572046, 51590902), Science and Technology Commission of Shanghai Municipality (16JC1400700), Innovation Program of Shanghai Municipal Education Commission (2017-01-07-00-03-E00055), and the Fundamental Research Funds for the Central Universities (2232019A3-02). J.Q. appreciates support from the Fundamental Research Funds for the Central Universities and Graduate Student Innovation Fund of Donghua University (CUSF-DH-D-2018002 and BCZD2019001).

Conflict of Interest

The authors declare no conflict of interest.

Keywords

aligned conductive nanowires, biodegradable elastomeric polyesters, hybrid electrodes, large-grained films, perovskite solar cells

Received: April 4, 2020
Revised: May 16, 2020
Published online: August 2, 2020

- [1] National Renewable Energy Laboratory, Best research-cell efficiencies chart, <https://www.nrel.gov/pv/cell-efficiency.html> (accessed: March 2020).
- [2] A. Mershin, K. Matsumoto, L. Kaiser, D. Yu, M. Vaughn, M. K. Nazeeruddin, B. D. Bruce, M. Graetzel, S. Zhang, *Sci. Rep.* **2012**, 2, 234.

- [3] S. Tian, J. Li, S. Li, T. Bu, Y. Mo, S. Wang, W. Li, F. Huang, *Sol. Energy* **2019**, 183, 386.
- [4] K. K. Sadasivuni, K. Deshmukh, T. N. Ahipa, A. Muzaffar, M. B. Ahamed, S. K. K. Pasha, M. A. A. Al-Maadeed, *J. Mater. Sci.* **2019**, 30, 951.
- [5] K. Zhu, Z. Lu, S. Cong, G. Cheng, P. Ma, Y. Lou, J. Ding, N. Yuan, M. H. Rummeli, G. Zou, *Small* **2019**, 15, 1902878.
- [6] L. Lu, Z. Yang, K. Meacham, C. Cvetkovic, E. A. Corbin, M. Xue, L. Yin, J. Boroumand, G. Pakeltis, T. Sang, K. J. Yu, D. Chanda, R. Bashir, R. W. Gereau, X. Sheng, J. A. Rogers, *Adv. Energy Mater.* **2018**, 8, 1703035.
- [7] H. Qiu, H. Cheng, J. Meng, G. Wu, S. Chen, *Angew. Chem., Int. Ed.* **2020**, 59, 7934.
- [8] N. Kim, H. Kang, J. H. Lee, S. Kee, S. H. Lee, K. Lee, *Adv. Mater.* **2015**, 27, 2317.
- [9] M. Zhang, S. L. Fang, A. A. Zakhidov, S. B. Lee, A. E. Aliev, C. D. Williams, K. R. Atkinson, R. H. Baughman, *Science* **2005**, 309, 1215.
- [10] M. Song, D. S. You, K. Lim, S. Park, S. Jung, C. S. Kim, D. H. Kim, D. G. Kim, J. K. Kim, J. Park, Y. C. Yang, J. Heo, S. H. Jin, J. H. Park, J. W. Kang, *Adv. Funct. Mater.* **2013**, 23, 4177.
- [11] F. Selzer, N. Wei, D. Knepp, L. Bormann, C. Sachse, N. Gaponik, A. Eyckmüller, K. Leo, L. Müller-Meskamp, *Nanoscale* **2015**, 7, 2777.
- [12] W. Xiong, H. Liu, Y. Chen, M. Zheng, Y. Zhao, X. Kong, Y. Wang, X. Zhang, X. Kong, P. Wang, *Adv. Mater.* **2016**, 28, 7167.
- [13] Y. Lee, S. Y. Min, T. S. Kim, S. H. Jeong, J. Y. Won, H. Kim, W. Xu, J. K. Jeong, T. W. Lee, *Adv. Mater.* **2016**, 28, 9109.
- [14] T. Kim, Y. W. Kim, H. S. Lee, H. Kim, W. S. Yang, K. S. Suh, *Adv. Funct. Mater.* **2013**, 23, 1250.
- [15] J. V. D. Groep, P. Spinelli, A. Polman, *Nano Lett.* **2012**, 12, 3138.
- [16] R. M. Mutiso, M. C. Sherrott, A. R. Rathmell, B. J. Wiley, K. I. Winey, *ACS Nano* **2013**, 7, 7654.
- [17] Y. Wang, G. A. Ameer, B. J. Sheppard, R. Langer, *Nat. Biotechnol.* **2002**, 20, 602.
- [18] I. Pomerantseva, N. Krebs, A. Hart, C. M. Neville, A. Y. Huang, C. A. Sundback, *J. Biomed. Mater. Res., Part A* **2009**, 91A, 1038.
- [19] J. Dey, H. Xu, J. Shen, P. Thevenot, S. R. Gondi, K. T. Nguyen, B. S. Sumerlin, L. Tang, J. Yang, *Biomaterials* **2008**, 29, 4637.
- [20] M. J. N. Pereira, B. Ouyang, C. A. Sundback, N. Lang, I. Friebs, S. Mureli, I. Pomerantseva, J. McFadden, M. C. Mochel, O. Mwizerwa, *Adv. Mater.* **2013**, 25, 1209.
- [21] Q. Liu, L. Jiang, R. Shi, L. Zhang, *Prog. Polym. Sci.* **2012**, 37, 715.
- [22] H. Cheng, P. S. Hill, D. J. Siegwart, N. Vacanti, A. K. R. Lytton Jean, S. W. Cho, A. Ye, R. Langer, D. G. Anderson, *Adv. Mater.* **2011**, 23, H95.
- [23] J. Yang, C. Bao, K. Zhu, T. Yu, Q. Xu, *ACS Appl. Mater. Interfaces* **2018**, 10, 1996.
- [24] Y. Lee, M. Suh, D. Kim, D. Lee, H. Chang, H. S. Lee, Y. W. Kim, T. Y. Kim, K. S. Suh, D. Y. Jeon, *Adv. Funct. Mater.* **2014**, 24, 6465.
- [25] J. Xu, J. Xia, S. W. Hong, Z. Lin, F. Qiu, Y. Yang, *Phys. Rev. Lett.* **2006**, 96, 066104.
- [26] N. Murisic, L. Kondic, *J. Fluid Mech.* **2011**, 679, 219.
- [27] E. M. Freer, O. Grachev, D. P. Stumbo, *Nat. Nanotechnol.* **2010**, 5, 525.
- [28] S. Kang, T. Kim, S. Cho, Y. Lee, A. Choe, B. Walker, S. J. Ko, J. Y. Kim, H. Ko, *Nano Lett.* **2015**, 15, 7933.
- [29] A. Tao, F. Kim, C. Hess, J. Goldberger, R. R. He, Y. G. Sun, Y. N. Xia, P. D. Yang, *Nano Lett.* **2003**, 3, 1229.
- [30] E. Adachi, A. S. Dimitrov, K. Nagayama, *Langmuir* **1995**, 11, 1057.
- [31] R. D. Deegan, O. Bakajin, T. F. Dupont, G. Huber, S. R. Nagel, T. A. Witten, *Nature* **1997**, 389, 827.
- [32] X. Li, B. Li, M. He, W. Wang, T. Wang, A. Wang, J. Yu, Z. Wang, S. W. Hong, M. Byun, S. Lin, H. Yu, Z. Lin, *ACS Appl. Mater. Interfaces* **2018**, 10, 4961.
- [33] V. K. Lamer, R. H. Dinegar, *J. Am. Chem. Soc.* **1950**, 72, 4847.

- [34] V. K. LaMer, *Ind. Eng. Chem.* **1952**, 44, 1270.
- [35] T. Sugimoto, *J. Colloid Interface Sci.* **2007**, 309, 106.
- [36] N. T. K. Thanh, N. Maclean, S. Mahiddine, *Chem. Rev.* **2014**, 114, 7610.
- [37] A. Poglitsch, D. Weber, *J. Chem. Phys.* **1987**, 87, 6373.
- [38] J. Qiu, Y. Qiu, K. Yan, M. Zhong, C. Mu, H. Yan, S. Yang, *Nanoscale* **2013**, 5, 3245.
- [39] P. W. Liang, C. Y. Liao, C. C. Chueh, F. Zuo, S. T. Williams, X. K. Xin, J. Lin, A. K. Y. Jen, *Adv. Mater.* **2014**, 26, 3748.
- [40] Y. Li, L. Meng, Y. Yang, G. Xu, Z. Hong, Q. Chen, J. You, G. Li, Y. Yang, Y. Li, *Nat. Commun.* **2016**, 7, 10214.
- [41] P. Liu, W. Wang, S. Liu, H. Yang, Z. Shao, *Adv. Energy Mater.* **2019**, 9, 1803017.
- [42] D. Yang, R. Yang, K. Wang, C. Wu, X. Zhu, J. Feng, X. Ren, G. Fang, S. Priya, S. Liu, *Nat. Commun.* **2018**, 9, 3239.
- [43] M. Saliba, T. Matsui, K. Domanski, J. Y. Seo, A. Ummadisingu, S. M. Zakeeruddin, J. P. Correa-Baena, W. R. Tress, A. Abate, A. Hagfeldt, M. Grätzel, *Science* **2016**, 354, 206.
- [44] W. S. Yang, B. W. Park, E. H. Jung, N. J. Jeon, Y. C. Kim, D. U. Lee, S. S. Shin, J. Seo, E. K. Kim, J. H. Noh, S. Seok, *Science* **2017**, 356, 1376.
- [45] J. Zhao, Y. Deng, H. Wei, X. Zheng, Z. Yu, Y. Shao, J. E. Shield, J. Huang, *Sci. Adv.* **2017**, 3, 5616.
- [46] R. Rai, M. Tallawi, A. Grigore, A. R. Boccaccini, *Prog. Polym. Sci.* **2012**, 37, 1051.
- [47] D. Yang, R. Yang, J. Zhang, Z. Yang, S. Liu, C. Li, *Energy Environ. Sci.* **2015**, 8, 3208.
- [48] Y. Wang, Y. M. Kim, R. Langer, *J. Biomed. Mater. Res. A* **2003**, 66, 192.
- [49] L. Wang, D. Chen, K. Jiang, G. Shen, *Chem. Soc. Rev.* **2017**, 46, 6764.
- [50] N. W. S. Wan, M. A. K. M. Hanafiah, *Bioresour. Technol.* **2008**, 99, 3935.